Effects of yttrium content on solidification, microstructure, and mechanical properties of laser powder bed fused IN718 superalloy

Thaviti Naidu Palleda [1, 2, *], Hasina Tabassum Chowdhury [1], Santhosh Banoth [1, 2], Hideyuki Murakami [2, 3], Koji Kakehi [1, *]

1. Department of Mechanical Systems Engineering, Tokyo Metropolitan University, 6-6, Asahigaoka, Hino-shi, Tokyo 191-0065, Japan
2. Research Center for Structural Materials, National Institute for Materials Science, 1-2-1, Sengen, Tsukuba-City 305-0047, Japan.
3. Department of Nanoengineering and Nanoscience, Waseda University, Tokyo 169-8555, Japan

Abstract

The microstructural evolution and mechanical properties of IN718 superalloy with different yttrium (Y) contents were investigated. In this study, three alloys containing 0wt%, 0.07wt%, and 0.58wt% of Y were fabricated by laser powder bed fusion (L-PBF). The experimental results showed that with a minor addition of Y content (0.07wt%), the tensile ductility at 650 ºC increased from 10.3% to 20.3%, and the creep life increased from 203h to 1545h. The increased tensile ductility and creep life are attributable to the formation of fine MC carbides, which induce serrated grain boundaries, and to the strong affinity of Y for oxygen, resulting in the formation of Y_2O_3 to strengthen the grain boundaries. However, when the Y addition increased (0.58wt%), the formation of a large Y-rich phase at the grain boundary reduced the tensile ductility and creep life.

Keywords: Ni-based superalloy, Yttrium, Laser powder bed fusion, MC carbides, Tensile and creep properties

* Corresponding authors: Thaviti Naidu Palleda, Department of Mechanical Systems Engineering, Tokyo Metropolitan University, 6-6, Asahigaoka, Hino-shi, Tokyo 191-0065, Japan;
Tel.: + 81-080-9533-5898; Email address: ptnaidu@tmu.ac.jp

Koji Kakehi, Department of Mechanical Systems Engineering, Tokyo Metropolitan University, 6-6, Asahigaoka, Hino-shi, Tokyo 191-0065, Japan;
Tel.: + 81-426-771-712; Email address: kkakehi@tmu.ac.jp

1. Introduction

In the last decade, metal additive manufacturing (MAM) has gained great prominence as an essential manufacturing technique due to its ability to fabricate parts with near-net shapes [1]. Among several MAM techniques, selective laser melting (SLM) is promising for fabricating complex metal parts with high precision; it involves the gradual melting of fine metallic powders layer by layer, guided by a geometry-directed laser beam [2]. However, the susceptibility to ductility loss at high temperatures due to powder contamination poses a critical challenge to the industrial application of SLM parts. Numerous studies have reported that impurity elements, notably the levels of oxygen and sulfur, can exert a significant influence on the quality of the build, the microstructure, and the mechanical properties at elevated temperatures, even when present at low concentrations [3][4][5][6][7]. The excessive oxygen and sulphur may alter the molten pool dynamics and cause issues like spattering and balling effects during PBF processing, leading to poor build quality [3][8][9]. Furthermore, when Ni-based superalloys are processed using L-PBF, the resulting materials exhibit lower tensile and creep ductility at high temperatures compared to cast and wrought alloys. The decrease in ductility can be attributed to high-temperature embrittlement, which occurs due to the dynamic segregation of embrittling elements such as oxygen (O) and sulfur (S) to the grain boundaries and crack tips under applied load [5][6][7][10][11][12]. On other hand, the higher oxygen content could potentially influence the microstructure by changing the alloy composition by oxide formation and thus lead to inferior creep properties. For instance, the formation of oxides in IN718 alloy consumes γ' forming element such as Al and Ti in the matrix. This process destabilizes γ' $Ni_3(Al,Ti)$ and accelerates the conversion reaction of γ'' to δ phase at the interdendritic regions during heat treatment. The higher interdendritic δ phases ultimately lead to inferior creep properties [4]. Therefore, controlling impurity concentrations in both the starting powders and AM processing is critical to achieving superior mechanical properties, especially at high temperatures.

Traditionally, counteracting impurities like oxygen and sulfur in Ni-based superalloys involved the addition of micro-alloying elements such as Zr, B, Hf, Ca, Mg, and rare earth elements [13][14][15]. These elements act as impurity scavengers and improve high-temperature mechanical properties, especially creep properties. Rare earth elements have been widely employed in various alloys, including steels [16], Ni-based super alloys [17][18], and

high-entropy alloys (HEAs) [19][20], to improve metallurgical quality [17], mechanical properties [21][22], and oxidation resistance[23][24]. Among all rare earth elements, yttrium (Y) is a reasonable choice for controlling oxygen content, as it has a high oxygen scavenging capability and relatively low costs. The deoxidizing and desulphurizing effects of Y in conventionally cast and wrought Ni-based superalloys are well known. Due to its strong affinity for oxygen and sulphur, Y can easily form highly stable oxides (Y_2O_3) and oxy-sulphides (Y_2O_2S or Y_2S_3), which reduce impurity segregation at the grain boundary and purify the grain boundary [25][26]. In addition, owing to its larger atomic size and lower solubility in the γ-matrix, Y preferentially tends to enrich at the grain boundaries, leading to grain boundary cohesive strengthening and the refinement of grain boundary carbides, which result in superior creep properties. Many studies reported that the room temperature tensile ductility of superalloys could be significantly increased via minor Y addition owing to grain boundary purification [25] and grain refinement [27][28]. Zhou et al. revealed that the optimal incorporation of yttrium (Y) can significantly enhance the stress-rupture life of the M951 superalloy by transforming the grain boundary carbide structure from a continuous network into a discrete granular morphology [22]. Moreover, many works reported that Y micro-alloying is indeed effective in improving oxidation resistance by increasing the adhesion and resistance to the spalling of the oxide layer [23].

The aforementioned studies imply that the optimal addition of Y can significantly improve the high-temperature mechanical properties of conventional Ni-based superalloys. However, there are few reports on the effect of Y addition in additively manufactured Ni-based alloys. In a previous study [29], we studied the effect of Y on the microstructure and high-temperature mechanical properties of SLM IN718 under conventional heat treatment conditions. Since the microstructure of SLM IN718 presents severe anisotropy due to the presence of a columnar-grained microstructure, homogenization heat treatment was employed in the present study. This study focuses on the effect of Y addition on solidification behavior, microstructure evolution, and tensile and creep properties.

2. Materials and experimental procedures

Cuboidal specimens of reference IN718 and Y-modified IN718, with dimensions of 45x45x45 mm, were prepared using an EOSINT M280 LPBF system (EOS GmbH, Krailling, Germany). This LPBF system was equipped with an Ytterbium fiber laser beam for the fabrication process. Gas atomization was used to produce pre-alloyed IN718 feedstock

powders. The nominal composition of these powders is detailed in Table 1, and the average particle size was approximately 63 μm. A set of optimized processing parameters was utilized, including a laser power of 400 W, a beam diameter of 100 μm, a scanning rate of 0.96 m/s, a layer thickness of 40 μm, an interlayer scanning angle of 66.5°, and a baseplate temperature of 80°C. These parameters were employed to fabricate fully dense specimens. The cuboidal block was sliced into 3-mm-thick plates, and specimens were machined along the building direction for microstructural and mechanical characterization using a wire electro-discharge machining system (WEDM, HS-300, Brother Industries Ltd., Japan). The specimens were subjected to homogenization, solution, and aging (HSA) heat treatments, as follows: homogenization at 1150ºC for 2h followed by air cooling, solution treatment at 980ºC for 1 h followed by air cooling, and a two-step aging treatment at 720ºC for 8 h followed by furnace cooling to 620ºC and holding for 10 h followed by air cooling. The specimens were encapsulated in vacuumed quartz ampoules to avoid oxidation at high temperatures. The heat treatment was performed in a box furnace (FT-105FM, FULL-TECH, Osaka, Japan).

For microstructural characterization, the specimens were hot mounted in epoxy resin, then underwent a sequential polishing process using 240-2000 SiC grit papers, followed by diamond suspension down to 3 μm. They were finally polished to a finish with 0.02 μm colloidal silica. This polishing procedure was carried out using a Struers automatic polishing machine (Tegramin-30, Struers LLC, Cleveland, OH, USA) automatic polishing machine. A field emission scanning electron microscope (FE-SEM, JSM-7200F, JEOL Ltd., Tokyo, Japan) equipped an energy-dispersive X-ray spectroscope detector (EDAX AMETEX 9424, Tokyo, Japan), was operated at an accelerated voltage of 15 kV. The grain structure and crystallographic texture were obtained using electron backscattered diffraction (EBSD; Oxford Instruments, Oxfordshire, UK). The EBSD scans were performed at 100x magnification with a step size of 1 μm and 4 μm for as-built, HSA (0.58Y) specimens and HSA(0Y,0.07Y) specimens, respectively. for each sample condition, at least two EBSD maps were acquired with scanning area of 1.5 x 3.0 mm^2. The EBSD data analysis was accomplished using TSL-OIM^{TM} software (EDAX Inc., USA). The grain dilation method of 5° grain tolerance angle and minimum grain size of 2 pixels was performed to clean up data. A critical misorientation of 2°-15° and >15° was used to define Low angle grain boundary (LAGBs) and high angle grain boundary (HAGBs), respectively. The CSL boundaries with 60° <111> (Σ3) and 38.9° <110> (Σ9) configuration were identified as annealing twin boundaries (TBs). The average grain size (grain diameter) was calculated excluding twin boundaries (TBs).

The mechanical testing was done on dog-bone-shaped specimens with gauge dimensions of 19.6x3x2.5 mm^3, sectioned parallel to the building direction. The high temperature (650 ^oC) tensile tests were performed at a constant strain rate of $1x10^{-3}$ s^{-1} by employing the Autograph AG-100kNE (Shimadzu Co., Kyoto, Japan) mechanical testing system with a load cell maximum capacity of 100 kN. The tensile testing system was equipped with a three-zone resistance heating furnace. The specimens were heated up to 650^oC at 10 ^oC/min and held for 30 min to obtain homogenous temperature distribution within the specimen. The temperature was measured and controlled by a K-type thermocouple mounted on the specimen. The strain measurements were conducted by a Kyowa DT-20D displacement transducer (Kyowa Electronic Instruments Co., Ltd, Tokyo, Japan) connected to Keyence wave logger data acquisition software (Keyence Corporation, Osaka, Japan). The constant-load tensile creep tests were performed at 650^oC using the RT-20 creep test system attached to a three-zone furnace. A constant load of 550 MPa was applied to the specimen using a fulcrum with a lever arm ratio of 1:10. The temperature was controlled within ±2^oC by a thermocouple (k-type) in direct contact with the specimen using a Bethel-4A temperature control system (Toshin Kogyo Co., Ltd., Tokyo, Japan). Strain measurements were continuously monitored by a linear variable differential transducer (LVDTs) (Peacock, ModelD-10S, Ozaki Mfg. Co. Ltd., Tokyo, Japan).

The differential thermal analysis (DTA) measurements were performed using a SETARAM Labsys instrument (Caluire et Cuire, France) to identify the phase transition temperatures. Before each DTA experiment, a blank run was conducted on a blank sample and reference samples (Indium) to obtain a baseline. Samples with a charge weight of 150-200 mg were used. The DTA runs were carried out in continuous heating/cooling mode with a constant rate of 10^oC /min and a 10 min isothermal hold between heating/cooling steps to allow the sample to thermally equilibrate. To avoid oxidation, argon gas was continuously flowed at a rate of 50 ml/min. The DTA thermograms were corrected by subtracting a baseline run with an empty Al_2O_3 crucible.

Table 1. Nominal chemical compositions of SLM 718 powders (wt%).

Alloy	**Ni**	**Cr**	**Fe**	**Nb**	**Mo**	**Ti**	**Al**	**C**	**Mn**	**Si**	**O***	**N***	**Y**
0Y	52.62	19.6	Bal.	5.05	2.85	1.10	0.46	0.04	0.13	0.02	190	76	-
0.07Y	52.07	18.93	Bal.	5.22	3.06	0.84	0.61	0.04	0.16	0.16	70	75	0.07

0.58Y	52.56	19.13	Bal.	5.13	3.08	0.86	0.63	0.05	0.14	0.16	142	54	0.58

*Oxygen and nitrogen are given in ppm

3. Results and discussion

3.1 Effects of Y on microstructure evolution and solidification.

The as-built microstructure shown in Fig. 1 exhibited the characteristic columnar grain structure associated with L-PBF–processed alloys owing to steep temperature gradients experienced during the processing. The interdendritic regions showed elemental segregation of Nb and the presence of Laves phase $(Ni,Fe.Cr)_2$ (Nb,Mo) characterized by a long strip-like morphology.. The phase fraction of Laves were measured to be 12.7%, 13.2%, and 20% for the Y-free, 0.07Y-added, and 0.58Y-added alloys, respectively. The higher Y addition (0.58wt.%) significantly increased amount of Laves phase and changed its morphology from an irregular blocky type (Fig.1g) to a large eutectic clustered morphology (Fig.1h and Table 2.). To investigate the effect of yttrium micro-alloying on solidification and segregation, Scheil simulations were conducted using Pandat software, utilizing the PanNi database. The Scheil model was used because the L-PBF process follows non-equilibrium solidification. During the solidification process of L-PBF of IN718, as the liquid melt temperature cools, the primary γ dendrite formation (L→L+γ at 1330 °C) starts in the early stages of solidification. As the liquid melt further cools, the growth of γ dendrites continues and the solute content of Nb accumulates in the interdendritic liquid due to their lower solubility in the γ matrix phase. The Nb content in the interdendritic liquid reached up to 16%, 14.9%, and 13% in the 0Y, 0.07Y, and 0.58Y added alloys, respectively (Fig.2 (b), (d), (f)). The elevated levels of Nb and C content within the interdendritic liquid promote the formation of NbC through a eutectic reaction: L→ L+γ+ NbC at 1233 °C. The NbC formation consumes Nb and most of C in the remaining liquid and shifts the liquid composition back to grow the γ dendrites further. As this process continues, the re-accumulation of Nb in the interdendritic liquid encourages the formation of Laves phase through another eutectic reaction: L→L+γ+Laves at 1160 °C. The formation of Laves phase at the dendritic region in the as-built microstructure is shown in Fig. 1(d-f). In both Y-free and Y-added alloys, the solidification process follows similar paths, i.e., L → γ+ L → γ + NbC + L → γ + Laves+ L. For Y-free alloy, the solidification terminates at 1153 °C (Fig. 2 (b)). However, in Y-added alloys, the solidification termination temperature is decreased to 1092 °C (Fig. 2 (d)), which suggest that the Y alloying delayed the solidification. Y has lower solubility (<0.1

at. % at 1250°C in Ni-alloy) and greater atomic size (1.80 Å); as a result, Y is rejected into the residual interdendritic liquid continuously, and the Y content in the final interdendritic liquid reached 8.5%, 6.5% in 0.07Y-alloy, 0.58Y-alloy respectively (Fig.2 (d), (f)). It is possible that the strong segregation of larger Y atoms in the interdendritic liquid prevented other elements from diffusion, thus delaying solidification. Y segregation promotes the formation of Y-rich $AlNi_8Y_3$ phase at the interdendritic region (Fig. 1 (i) and Table 2.) in later stages of solidification in Y-added alloys. However, from the predicted phase diagrams shown in Fig. 3 (c), it seems the $AlNi_8Y_3$ phase is transformed to Ni_5Y at temperatures below 790 °C. During solidification, the Nb content in the final interdendritic liquid was observed to decrease to 15%, 9%, and 7% for the alloys containing 0Y, 0.07Y, and 0.58Y, respectively (Fig. 2 (b), (d), (f)). The decrease in Nb is attributed to the formation of NbC and Laves phases during solidification. Though the thermodynamic modeling predicted δ phase formation at the final stage of solidification (Fig. 2(a), (c), (e)), no δ phase was observed in the as-built microstructure.

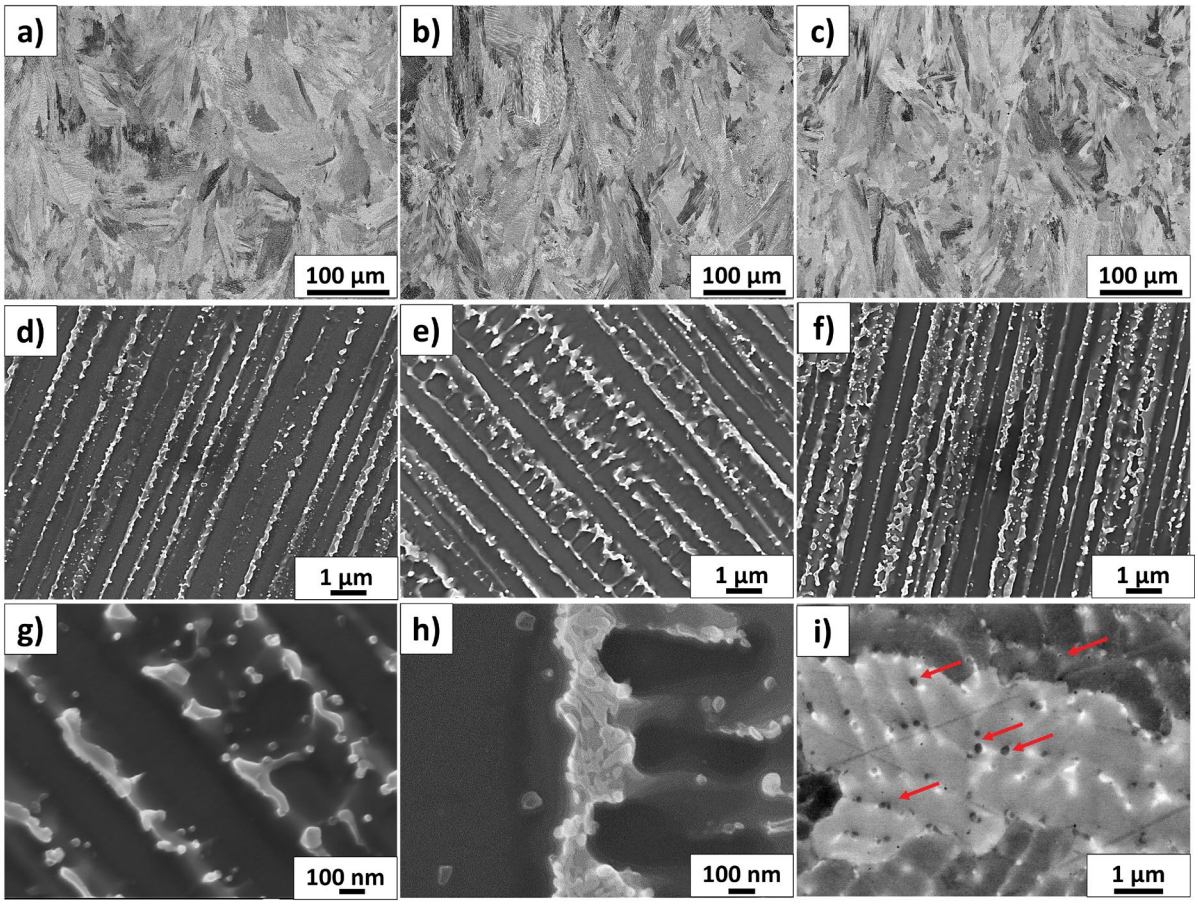

Fig. 1 SEM-BSE micrographs of LPBF-IN718 in as-built condition for (a), (d), (g) 0Y, (b), (e) 0.07Y, and (c), (f), (h), (i) 0.58Y specimens.(Red arrows indiacate Y-rich phases in 0.58Y unetched specimen).

Table 2. SEM-EDS compositional analysis for phases in 0Y, 0.58Y specimens in as-built condition.

Alloy	Element (at. %)	Ni	Al	Cr	Fe	Nb	Mo	Ti	Y
0Y	Laves	45.28	0.086	20.2	15.81	14.50	2.95	1.158	-
0.58Y	γ-Matrix	46.06	0.68	19.26	21.81	2.84	2.42	0.60	0.03
	Laves phase	43.15	0.72	14.30	15.32	11.73	2.56	1.37	2.68
	Y-rich phase	58.27	1.27	16.09	13.13	4.00	1.40	0.75	5.09

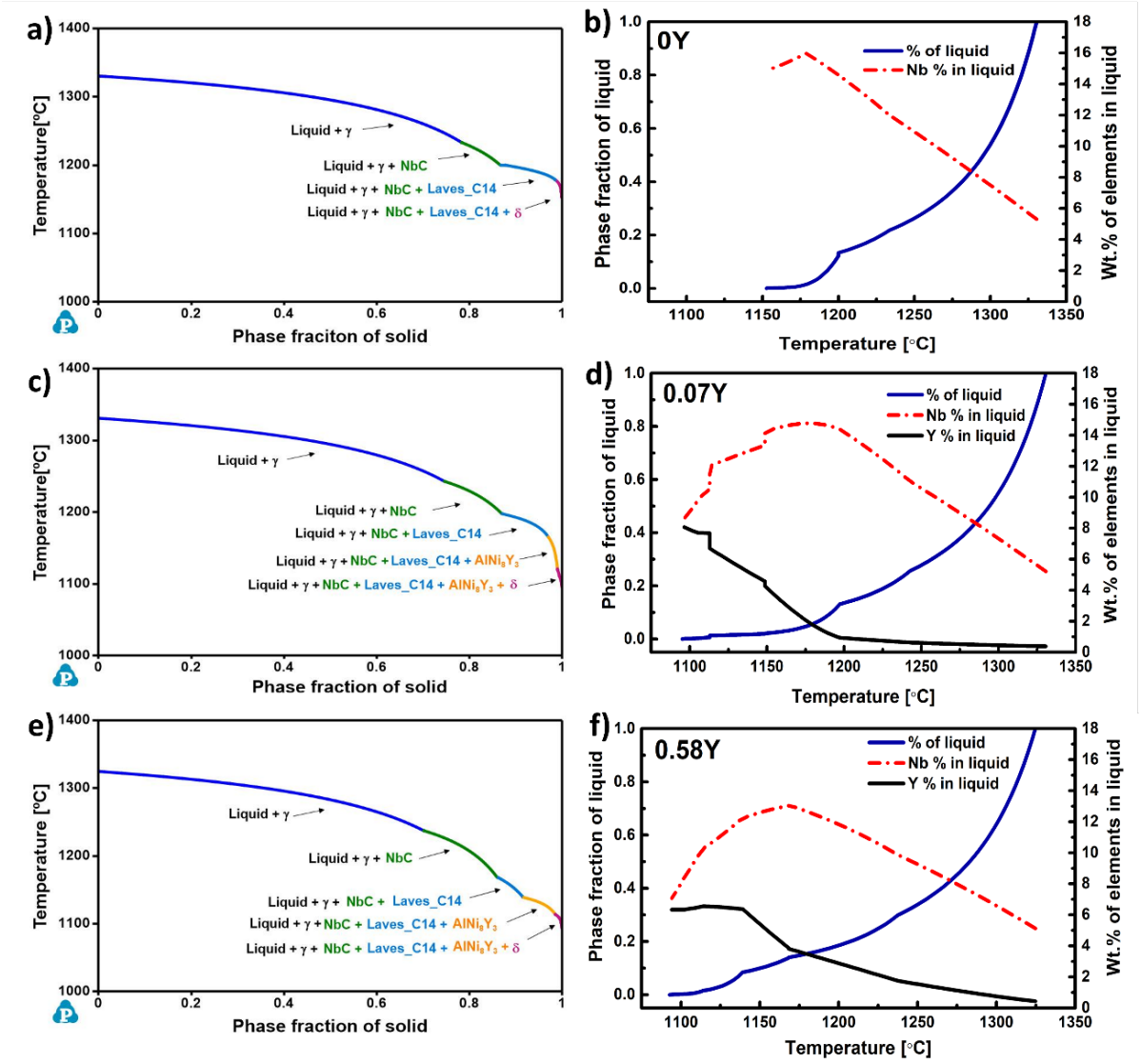

Fig. 2. The solidification sequences and segregation profiles of Y and Nb in the interdendritic liquid during solidification predicted using the Scheil model for (a)(b) 0Y, (c)(d) 0.07Y, and (e)(f) 0.58Y alloys.

.

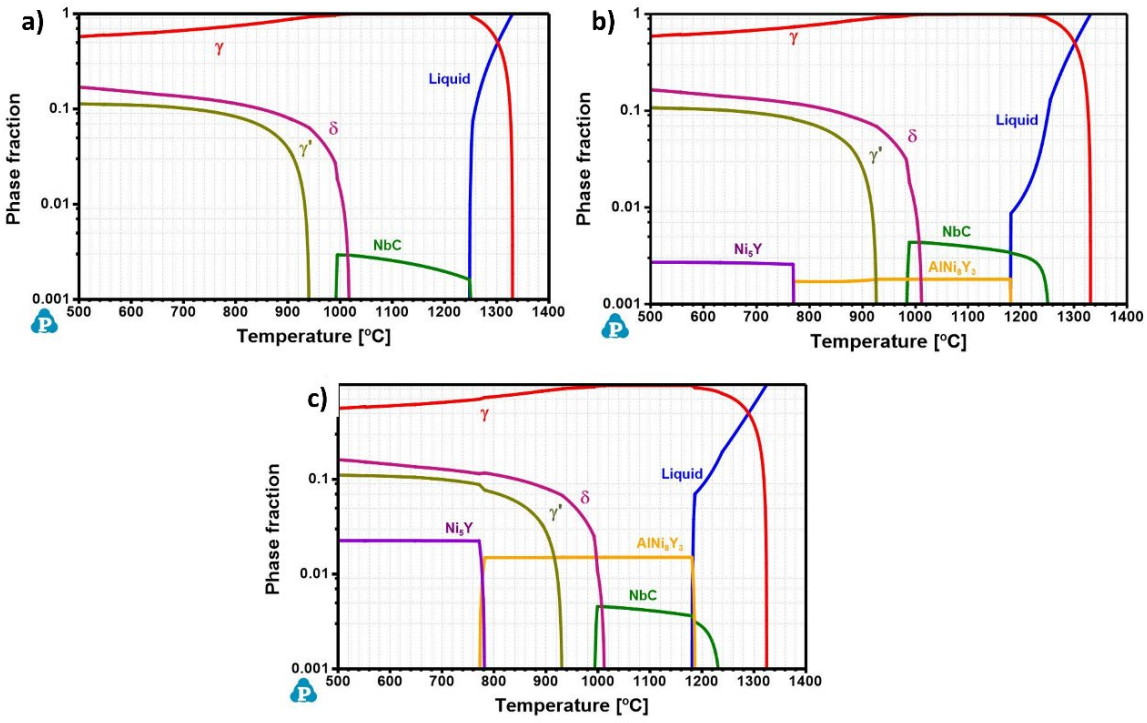

Fig. 3. Predicted equilibrium phase diagrams for different Y-added specimens (a) 0Y, (b) 0.07Y, (c) 0.58Y

Laves phase is considered detrimental to mechanical properties due to its brittle nature and nucleation of intergranular defects[30][31]. Further, the as-built microstructural features such as the columnar grain morphology, residual stress, and interdendritic segregation leads to anisotropic mechanical properties in SLM IN718 [32]. Therefore, a homogenization heat treatment is necessary to dissolve the Laves phase and mitigate Nb segregation. This process increases the volume fraction of strengthening γ′/γ″ precipitates during aging, consequently enhancing both tensile properties and creep resistance. Furthermore, the homogenization treatment induces recrystallization, resulting in the formation of coarse equiaxed grains. This effect contributes to a reduction in anisotropy and an improvement in creep life [33].

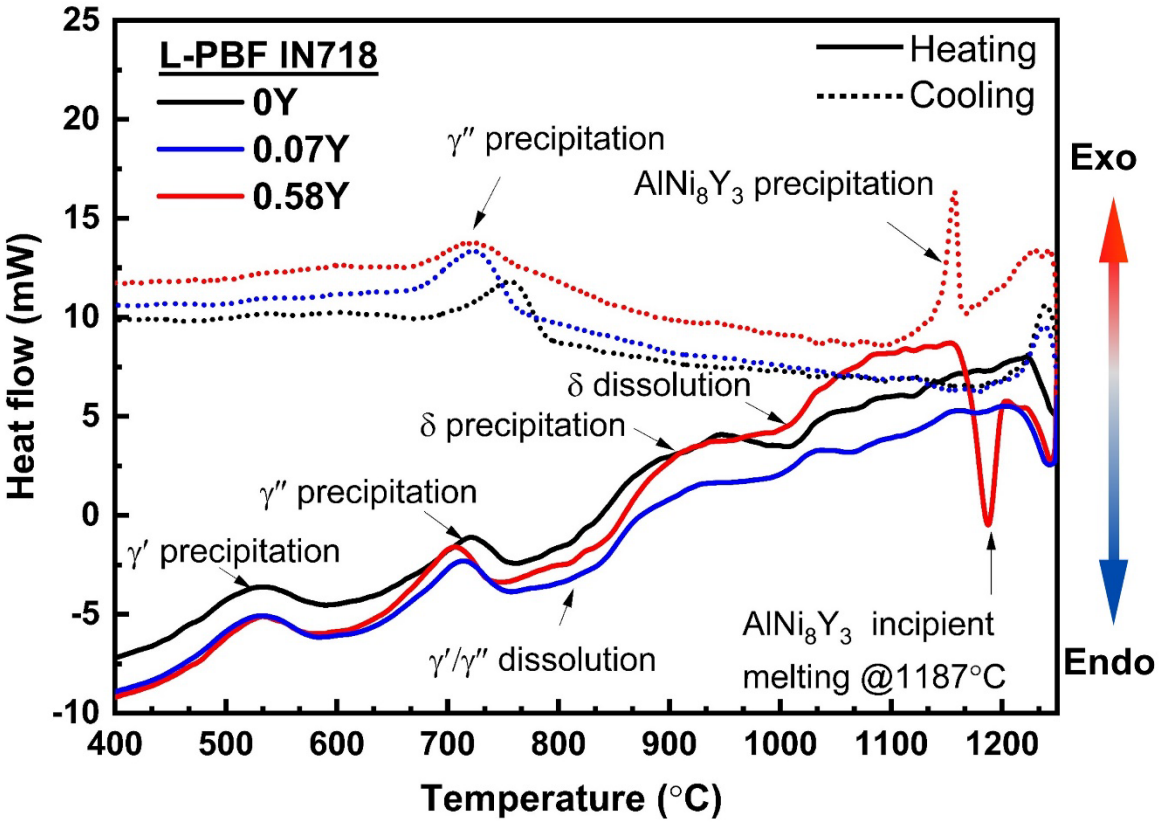

Fig. 4. Differential scanning calorimetry (DTA) curves of L-PBF IN718 obtained upon heating (solid lines) and cooling (dotted lines) for (a) 0Y, (b) 0.07Y, and (c) 0.58Y alloys. (Exo: Exothermic, Endo: endothermic)

The DTA measurements were conducted on as-built alloys to identify the critical temperature ranges for the dissolution of the secondary phases. The DTA thermographs shown in Fig. 4 reveal that γ' and γ″ form at temperatures of ~530 °C and ~720 °C, respectively. The dissolution valley of γ'/ γ″ precipitates occur in the temperature range of ~750-910°C. The δ phase forms in the temperature range of ~850-980°C either by the conversion of γ″ in to δ or by forming directly from γ-matrix. The valley in the temperature range ~1010-1040°C representing δ phase dissolution. For the 0.58Y-added alloy, an additional sharp valley, which considered as the incipient melting of $AlNi_8Y_3$ phase, was observed at ~1187 °C. The DTA measurements are well consistent with the predicted step diagrams given in Fig. 2 and previous reports[34][35][36].Based on the DTA measurements, the homogenization heat treatment (HSA) at 1150 °C for 2 h was selected to ensure the complete dissolution of Laves phase, δ phase, Nb distribution, and the elimination of the columnar grained structure.

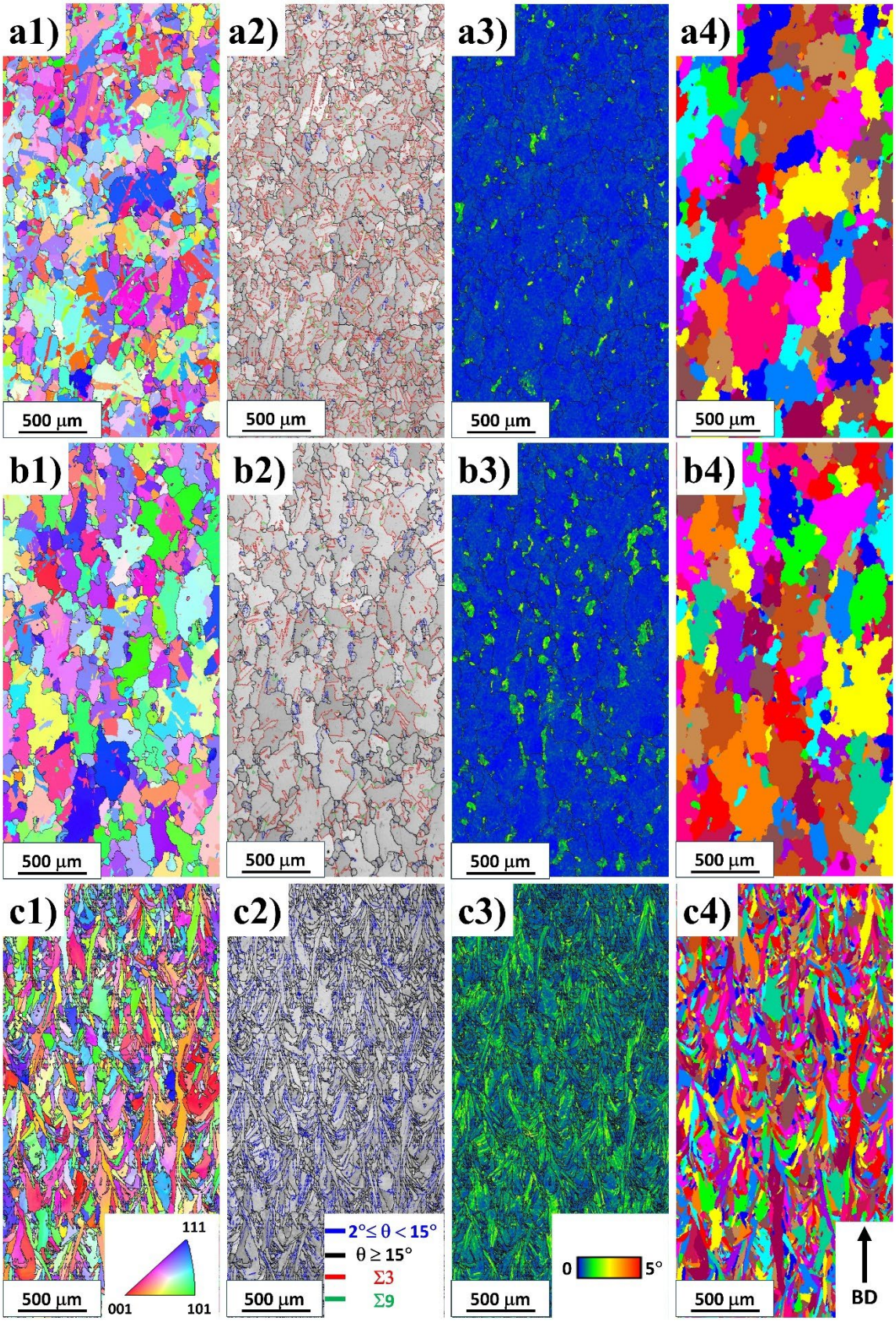

Fig. 5. EBSD analysis of HSA heat-treated specimen: (1) Inverse pole figure (IPF) maps, (2) Image quality (IQ) maps with the grain boundaries (GBs) and the twin boundaries (TBs), (3)

Kernel average misorientation (KAM) maps and (4) grain size maps for (a) 0Y, (b) 0.07Y, and (c) 0.58Y, respectively.

Figure 5 shows the EBSD analysis maps of Y-free and Y-added alloys in heat-treated condition. The Y-free alloy exhibited fully recrystallized and large equi-axed grains with random orientation (Fig. 5 a1, a3). The average grain size and the annealing twin fraction were calculated to be approximately 78 μm (including TBs ~29 μm) and 0.62, respectively (Fig. 5 a2, a4). The 0.07Y-added alloy exhibited near-complete recrystallization and possessed large equiaxed grains with an average grain size of 65 μm (including TBs ~38 μm) and an annealing twin fraction of 0.39, respectively (Fig. 5 b1-b4). In contrast, the 0.58Y-added alloy still consisted of fine columnar grains elongated in the building direction as shown in Fig. 5 c1, c4. The average grain size is measured to be 16 μm approximately. The higher fraction of LAGBs (~0.29) and the KAM map as shown in Fig. 5 c3 and c4, indicates that no recrystallization occurred in the 0.58Y-added alloy.

Figure 6 shows BSE micrographs of HSA heat-treated condition, revealing the complete dissolution of the initial cellular-dendritic solidification microstructure. The (Nb,Ti)-rich MC carbides (Fig. 7 (a)) were observed in the Y-free alloy. These carbides are blocky in shape and mostly present within the grain interior. In the 0.07Y-added alloy, on the other hand, fine carbides were observed both along the grain boundary and within the grain interior. These carbides are rich in Nb, Ti, and Y, as shown in Fig. 7 (b) and Table 3. The vertical “stone wall” arrangement of fine intragranular (Nb,Ti)C particle as shown in Fig. 6 (e) (indicated by white dotted arrows) is reminiscent of the previous as-built grain structure. In addition, uniform distribution of round/lenticular Y-rich phase was observed in the 0.58Y-added alloy at subgrain/grain boundaries. The precipitates were rich in Ni and Y (Fig. 7 (c) and Table 3). The statistical results presented in Table 4 suggest that the number density and area fraction of (Nb,Ti) C particles increases with increasing Y addition, while the particle size becomes finer. As mentioned earlier, Y tends to accumulate at the interdendritic/grain boundary regions during solidification. The higher Y concentration leads to the earlier formation of Y-rich phases during subsequent heat treatment. These Y-rich phases act as heterogeneous sites for NbC formation, increasing the area fraction of NbC precipitates. The higher number density and refinement of (Nb,Ti) C with Y addition is attributed to carbide fragmentation. Zhou et al. [37] reported that some Nb atoms in (Nb,Ti)C particles are substituted by Y. This substitution induces lattice distortion in (Nb,Ti)C particles due to Y's larger atomic size, ultimately leading to

fragmentation of these particles. Additionally, the inclusion of Y reduces the driving force for carbide formation by elevating the strain energy at the interface between (Nb,Ti)C particles and the γ-matrix, consequently leading to a higher number density of fine (Nb,Ti)C particles in Y-added alloys. Y addition results in grain growth inhibition due to the combined effects of Zener pinning and solute drag. However, the significance of each factor depends on constitute phases and composition of the alloys. In the 0.07Y-added alloy, the high density of fine NbC particles solely contribute to the Zener pinning along the grain boundary. Conversely, in the 0.58Y-added alloy, both NbC and the Y-rich phases impend the grain boundary mobility and leading to the Zener pinning effect. Furthermore, the increased Y content would induce solute drag effect in 0.58Y-added alloy. Due to larger atomic size of Y (1.80 Å) compared to Ni (1.24 Å)[38], Y preferentially tends to segregate along the grain boundary [39][40]. The grain boundary segregation of Y provides strong solute drag force and hinder the grain growth in 0.58Y-added alloy. Both Zener pinning of NbC, the Y-rich phases along with the solute drag of Y, elucidates the persistence of columnar grain structure in the 0.58Y-added alloy.

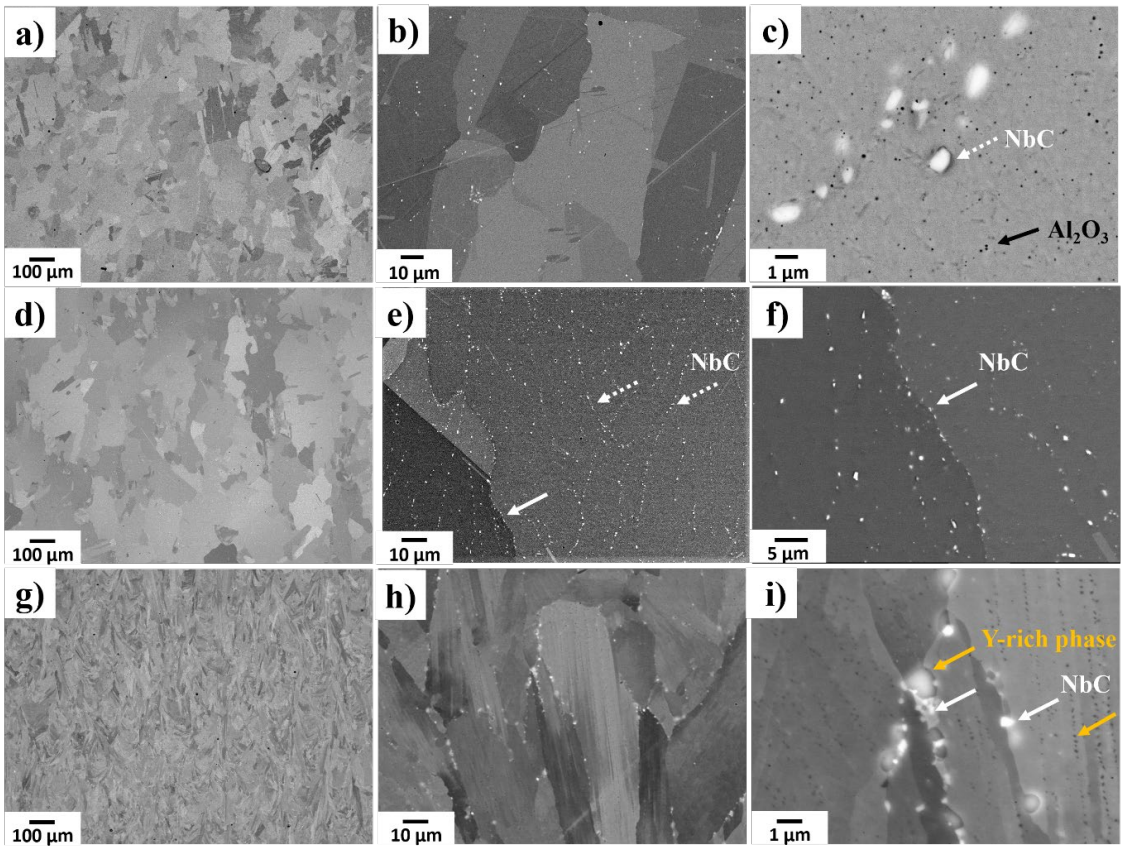

Fig. 6. BSE micrographs of the HSA heat-treated specimens of (a), (b), (c) 0Y, (d), (e), (f) 0.07Y (g), (h), (i) 0.58Y (the white solid arrows indicates intergranular NbC, and the white dotted arrows indicates intragranular NbC).

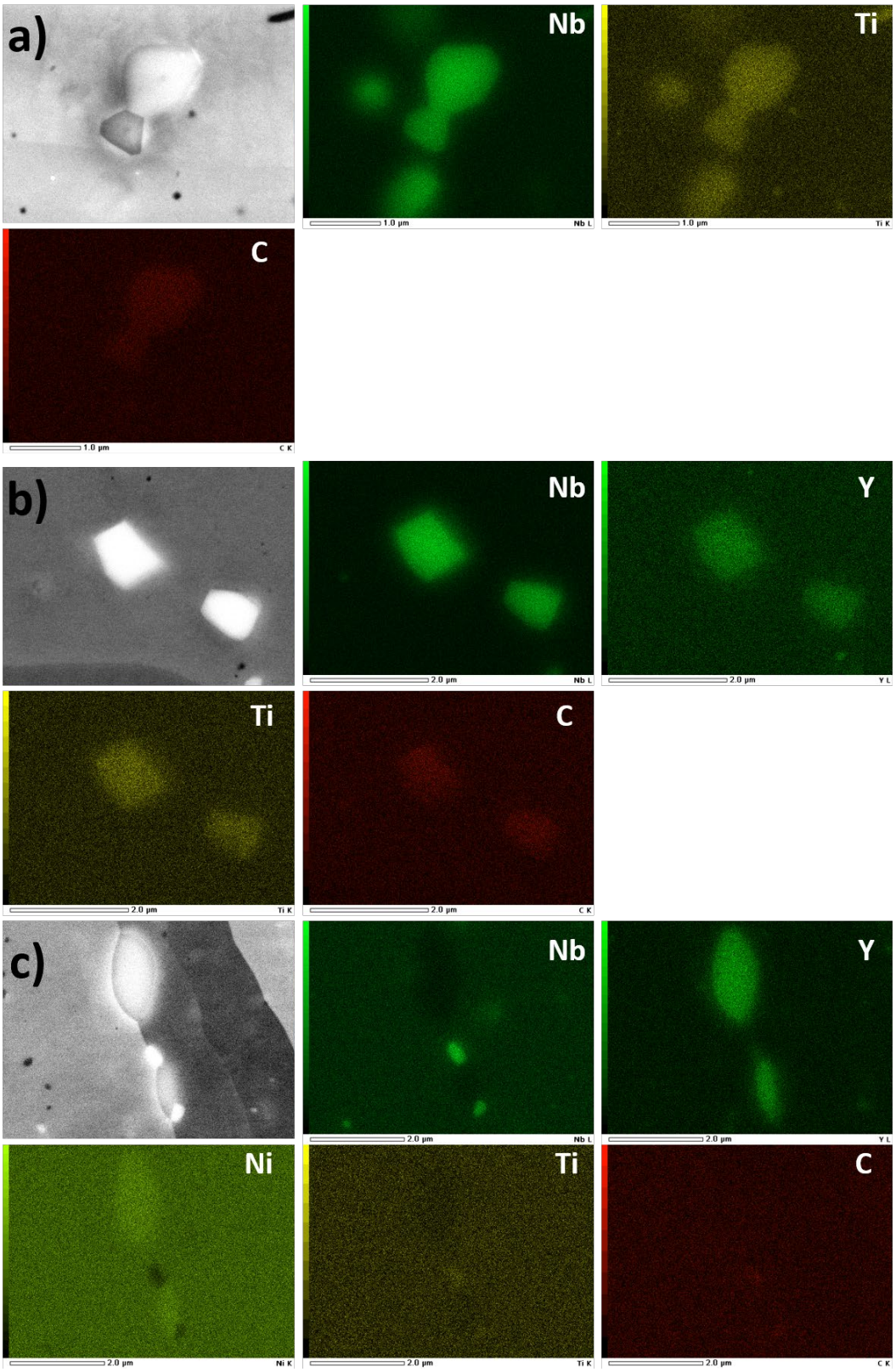

Fig. 7 SEM-EDS maps of HSA heat-treated IN718 for a) 0Y specimen showing NbC formation, b) 0.07Y specimen showing NbC formation, and c) 0.58Y specimen showing NbC formation adjacent to the Y-rich phase.

Table 3 SEM-EDS point analysis showing the elemental composition of phases in HSA heat-treated 0.58Y specimen.

Element (at. %)	Ni	Al	Cr	Fe	Nb	Mo	Ti	Si	C	Y
Matrix (γ)	51.66	1.06	17.68	14.77	2.25	1.47	0.88	1.30	27.45	0.04
Carbide (NbC)	19.28	0.38	8.99	7.07	29.55	0.46	4.55	0.37	27.45	0.10
Y-rich phase	64.63	1.59	3.75	5.04	1.87	0.25	0.29	3.79	6.20	11.38

Table 4. Statistics of area fraction, average size of NbC, and Y-rich phases in different Y content added specimens.

Specimen	Area fraction (%)		Average size (μm)	
	NbC	**Y-rich phase**	**NbC (blocky shape)**	**Y-rich phase (round/lenticular)**
0Y	0.25 ± 0.13	-	0.85 ± 0.32	-
0.07Y	0.53 ± 0.11	-	0.67 ± 0.28	-
0.58Y	0.96 ± 0.60	1.7 ± 0.3	0.43 ± 0.20	1.23 ± 0.52 (intergranular) 0.22 ± 0.06 (intragranular)

3.2 Effects of Y on mechanical properties.

Figure 8 presents the tensile test results for Y-free and Y-added alloys at 25℃ and 650℃ in as-built and HSA heat-treated conditions. The corresponding tensile properties, such as yield strength, ultimate tensile strength, and elongation, are listed in Tables 5 and 6. In the as-built condition, the 0.07Y-added alloy exhibited similar tensile properties to Y-free alloy at both 25℃ and 650℃. Nevertheless, the strengths were substantially improved in the 0.58Y-added alloy. This was attributable to the increased fractions of Laves phase and Y-rich phase in the same alloy. In the HSA heat-treated condition, Y addition contributed to the improvement in strength. At 25℃, the yield strengths of 0.07Y-added and 0.58Y-added alloys improved by 47 MPa and 196 MPa, respectively. This strength improvement would be mainly attributable to the higher fractions of fine carbides and Y-rich phase. With the increase in Y addition, the

fraction of fine carbides in the alloys increases, restricting grain boundary migration and limiting dislocation movement within the matrix. The Y-free and 0.07Y-added alloys showed almost the same elongation of 20%. This suggests that the minor addition of Y did not affect elongation much at 25℃. However, the higher Y addition resulted in a significant decrease in elongation. The elongation of 0.58Y-added alloy was measured to be 14.3%. The beneficial effect of Y addition on tensile properties was more prominent at 650℃. Figure 8 (c), (d) shows the tensile curves of the HSA heat-treated alloys at 650℃. The elongation of the 0.07Y-added alloy increased significantly, by 9.7%, which is twice that of the Y-free specimen. In the 0.58Y-added alloy, strength improved by 166 MPa, while elongation decreased by 5.7% compared to the Y-free specimen. The strain hardening capability of the 0.58Y-added alloy is higher at 25℃ compared to 650℃.This is due to the resistance provided by the brittle Y-rich phases to dislocation motion, which results in higher strain hardening. The dislocation interaction with intragranular Y-rich phase along the slip lines in the grain interior is shown in Fig.9c. During the deformation, the intragranular nano-sized Y-rich phases effectively pin the dislocations motion and results in strain hardening. On the other hand, the intergranular Y-rich phase merely act as load bearing constituent phases. During tensile deformation, because of large strain gradient between relatively soft γ-matrix and hard Y-rich phase results in the development of pulling stresses on the Y-rich phases. when these stresses are exceeded the fracture strength of Y-rich phase, the initial fracture occurs in the Y-rich phase (Fig. 9c), potentially initiating a crack within the surrounding γ-matrix and leading to intragranular facture. Nevertheless, at 650℃, the interface weakens in comparison to the Y-rich phase. This weakening promotes formation of cavities at the interface between γ-matrix and Y-rich phase well before the stress reaching the fracture threshold of the Y-rich phase. The formation of voids at the interface between γ-matrix and Y-rich phase can be seen in Fig. 9f. As the deformation continues, these voids tend to grow, leading to a gradual decrease in the strain hardening and intergranular fracture in 0.58Y-added alloy.

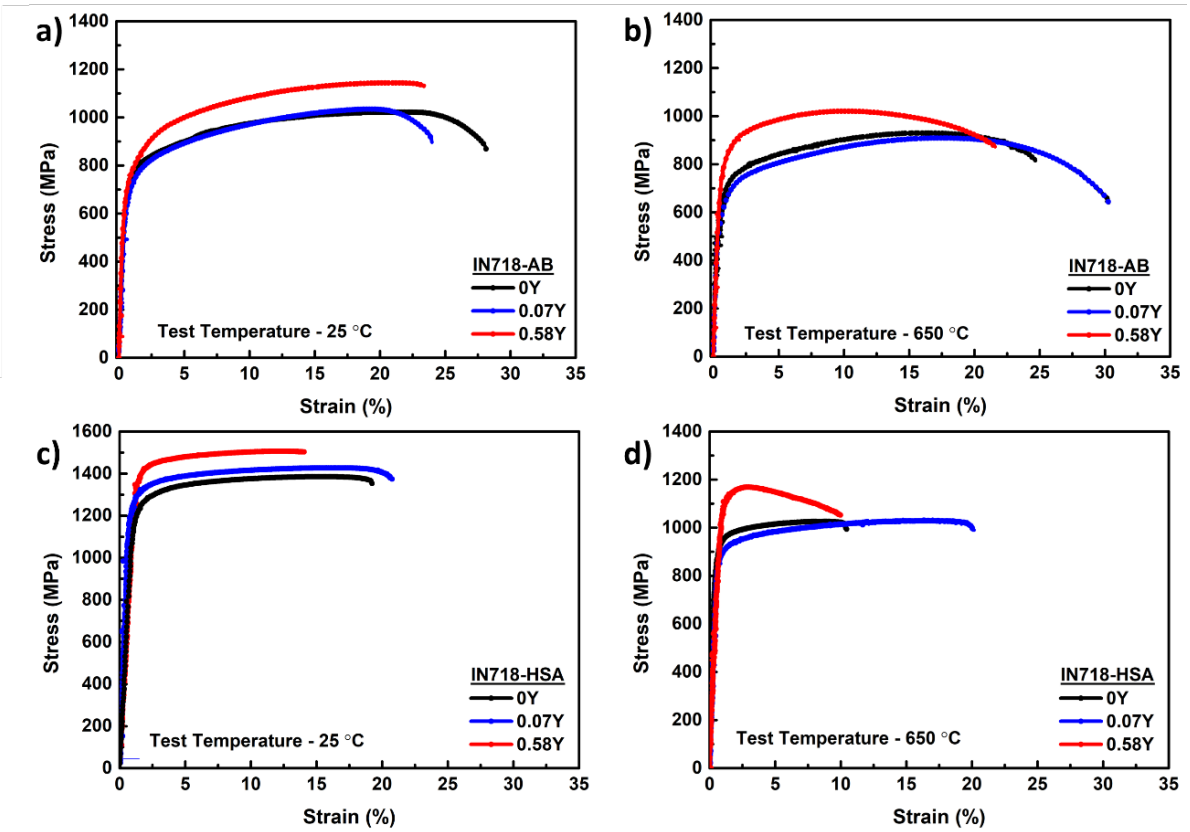

Fig. 8. Stress stain curves of (a), (b) as-built and (c), (d) HSA heat-treated specimens at 25°C and 650°C.

Table 5. Tensile properties of IN718 in as-built condition at 25°C and 650°C.

Alloy		Yield strength (MPa)	Tensile strength (MPa)	Elongation at fracture (%)
0Y	25°C	676	1022	28
	650°C	593	863	25
0.07 Y	25°C	666	1036	24
	650°C	600	859	29.3
0.58Y	25°C	693	1146	23.3
	650°C	796	1020	21.5

Table 6. Tensile properties of HSA heat -treated condition at 25°C and 650°C.

Alloy		Yield strength (MPa)	Tensile strength (MPa)	Elongation (%)
0Y	25°C	1203	1390	19.3
	650°C	930	1026	10.3
0.07Y	25°C	1250	1430	20.7
	650°C	876	1033	20.3
0.58Y	25°C	1399	1512	14.3
	650°C	1096	1170	9.9

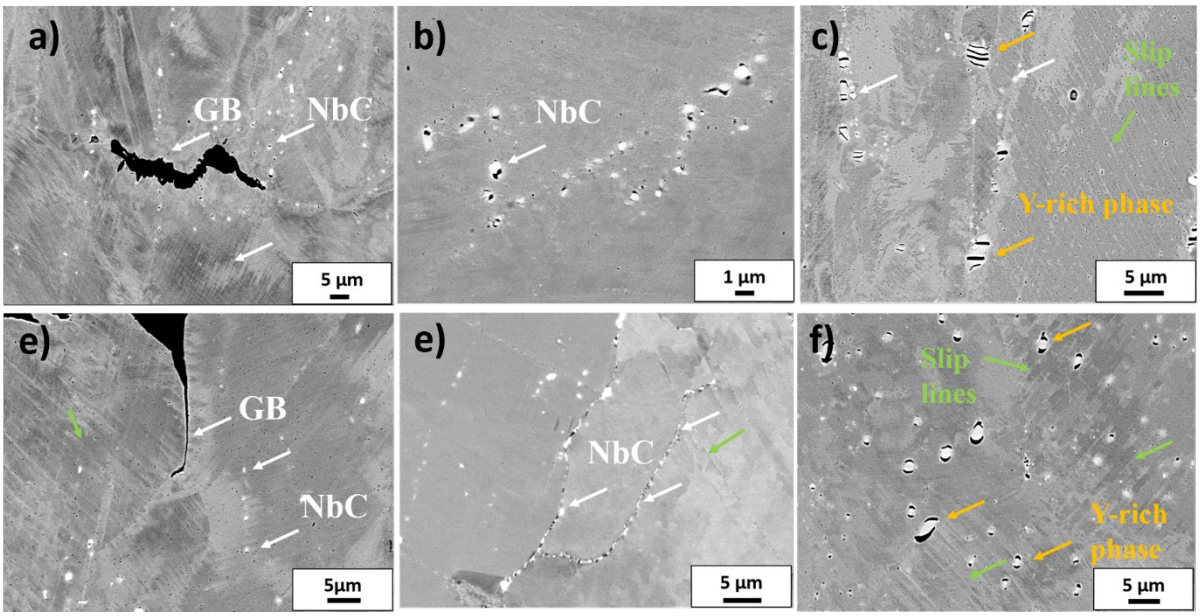

Fig. 9 SEM images of post-tensile deformation microstructures of HSA heat-treated specimens (a) 0Y, (b) 0.07Y, and (c) 0.58Y alloys at 25°C and (d) 0Y, (e) 0.07Y, and (f) 0.58Y alloys at 650°C

Figure 10 (a) shows the creep curves of Y-free and Y-added alloys in heat-treated condition. The creep tests were conducted at 650°C/550MPa. The correlations between creep rate and time are plotted in Fig. 10 (b). The corresponding quantitative creep properties are summarized in Table 7. As compared to the Y-free alloy, the 0.07Y-added alloy, having a higher density of fine intragranular and intergranular carbides, exhibited drastically higher creep life.

The creep life of 0.07Y-added alloy is 1543 h, which is approximately 7.5 times longer than that of the Y-free alloy (203 h). It is also observed that the 0.07Y-added alloy displayed a lower creep rate of, 6.30 x 10^{-10} s^{-1}. Nevertheless, higher Y addition (0.58%) reduced creep life sharply, to 293 h, and increased creep rate to 5.09 x 10^{-9} s^{-1}. The superior creep properties of the 0.07Y-added alloy would be attributable mainly to the presence of fine intergranular and intragranular NbC carbides as well as to the formation of Y_2O_3 [41]. The higher density of fine MC carbides within the grains is likely to interact with moving dislocations and restrict the dislocation motion effectively [42]. The creep rate of the 0.07Y-added alloy decreased compared to the Y-free alloy due to the suppression of dislocation movement caused by the interaction with fine carbides. Conversely, dislocation motion is easier in the Y-free alloy due to the presence of coarse and lower-density carbides, leading to a larger creep rate. Furthermore, the formation of fine intergranular carbides tends to create serrated grain boundaries, which in turn suppresses grain boundary sliding and delays the nucleation of creep voids and their interlinkage, preventing crack formation along the grain boundaries [43][44]. Thus, the onset of tertiary creep will be suppressed and prolong the creep life. The post-deformed microstructures of longitudinal sections of crept specimens are displayed in Fig. 11. In the Y-free alloy, the voids formed at the grain boundary. As the creep deformation continued, these voids gradually linked up, eventually forming the crack along the grain boundary. However, in the 0.07Y-added alloy, it is evident that that an array of voids nucleated at the intergranular MC carbides. However, the zig-zag grain boundary arrangement made it difficult for the void coalescence to develop into intergranular cracks, as shown in Fig. 11 (b). Thus, a slow rate of crack propagation along the grain boundary might be expected in the 0.07Y-added alloy. Furthermore, Fig. 11(c) reveals the formation of δ phase along the grain boundary and slip lines, which might be attributable to the thermomechanical aging that occurs during creep deformation. Due to prolonged (1545 h) thermal exposure at 650°C, the metastable γ″ would transform into the δ phase along the grain boundary during creep deformation. Additionally, its nucleation and growth are assisted by the high density of dislocations generated during creep deformation. The higher density of dislocations will facilitate the pathways, increase the efficiency of Nb diffusion to the grain boundary, and lead to the formation of a needle-shaped intergranular δ phase. There was also evidence that the δ phase formed along the slip lines, possibly associated with the shearing of γ″ precipitates. The shearing of γ″ precipitates forms stacking fault and promotes δ phase formation. However, no such transformation of γ″ into γ″ was observed in the Y-free alloy due to the shortened creep life. However, as shown in Fig. 10, the beneficial effect of Y on creep

properties was suppressed with excessive Y addition. Due to the smaller grain size and the presence of coarse, brittle Y-rich precipitates along the grain boundary, these factors would act as void nucleation sites and result in inferior creep properties.

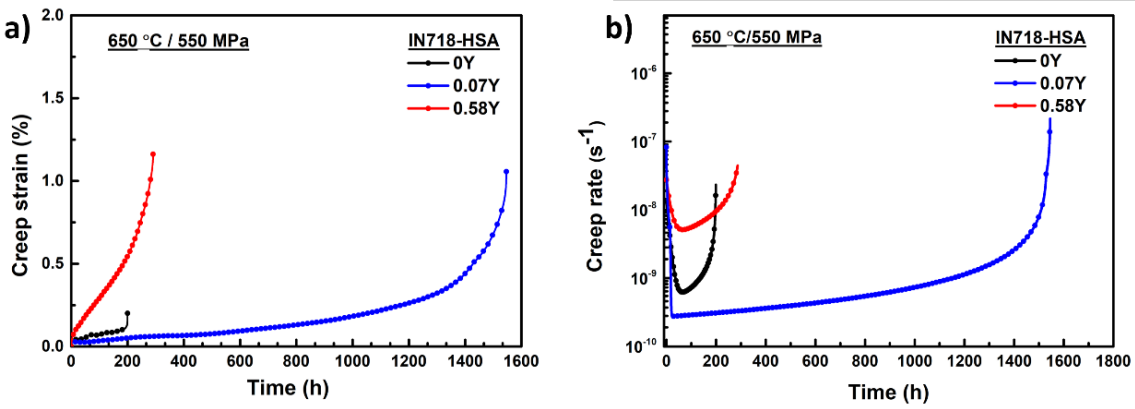

Fig. 10 Plots showing creep properties of Y-free and Y-added alloys in HSA heat-treated condition along the building direction: (a) illustrates the creep curves, while (b) demonstrates the correlations between creep rate and time.

Table 7 Creep properties of Y-free and Y-added alloys in HSA heat-treated condition.

Alloy	Creep life (h)	Creep elongation (%)	Min. creep rate (s^{-1})
0Y	203	0.2	6.30×10^{-10}
0.07Y	1545	1.03	2.73×10^{-10}
0.58Y	293	1.16	5.09×10^{-9}

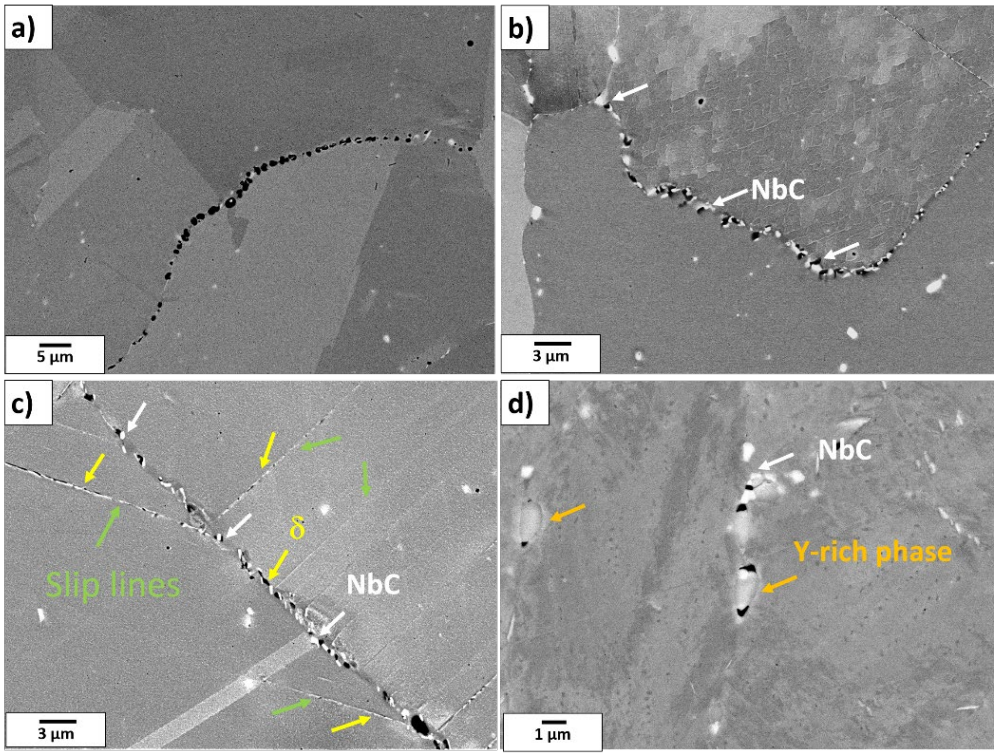

Fig. 11 SEM-BSE micrographs showing post-creep deformed microstructure of (a) 0Y and (b) 0.07Y specimens showing void formation and cracking of grain boundary NbC, (c) 0.07Y specimen showing formation of δ phase at the grain boundary and slip lines, and (d) 0.58Y specimen showing creep crack formation NbC and Y-rich phase phases at the grain boundary.

4. Conclusions

The microalloying effects of Y content on the solidification, microstructure, and mechanical properties of laser bed fused IN718 superalloy were studied, and the main conclusions are as follows:

1) Y addition significantly delays solidification.
2) Increasing the Y addition greatly enhances the formation of eutectic Laves phase and Y-rich phase at the interdendritic region during last stage of solidification.
3) During solidification, Y is continuously being expelled into the interdendritic liquid. As a result, the solute enrichment of Y in the interdendritic liquid occurs, which leads to the formation of Y-rich phase and the strong segregation of Y to the Laves phase.
4) Y addition promotes the formation of fine carbides along the grain boundary, grain interior, and Y_2O_3 by scavenging oxygen.
5) The formation of fine carbides at the grain boundaries led to serration of the boundaries and oxygen stabilization by Y_2O_3 formation, which significantly increased the high-

temperature tensile ductility and creep life in the specimen with only a small Y addition (0.07wt%).

6) However, higher Y addition resulted in inferior tensile ductility and creep life caused by the formation of a brittle Y-rich phase both at the grain boundary and inside the grain.

Declaration of Competing Interests

The authors declare that they have no known competing financial interests or personal relationships that could have appeared to influence the work reported in this paper.

Acknowledgments

This work was supported by the AMADA Foundation (AF-2018222-B3) and the JSPS KAKENHI (Grant Number 22H01366). Part of this work was supported by NIMS Joint Research Hub Program. The authors kindly thank Mr. Shao-yu Yen at National Cheng Kung University (NCKU), Taiwan, for helping with the Pandat software.

Author contributions

T.N.P. performed the experiments and analysis and wrote the first draft of the manuscript. H.T.C. and S.B. helped analyze the results and finalize the manuscript. H.M. and K.K. supervised the project. All authors discussed and commented on the manuscript.

Data availability

Data will be made available on request.

References

[1] L.E. Murr, S.M. Gaytan, D.A. Ramirez, E. Martinez, J. Hernandez, K.N. Amato, P.W. Shindo, F.R. Medina, R.B. Wicker, Metal Fabrication by Additive Manufacturing Using Laser and Electron Beam Melting Technologies, J Mater Sci Technol. 28 (2012) 1–14. https://doi.org/10.1016/S1005-0302(12)60016-4.

[2] W.E. Frazier, Metal additive manufacturing: A review, J Mater Eng Perform. 23 (2014) 1917–1928. https://doi.org/10.1007/s11665-014-0958-z.

[3] C.L.A. Leung, S. Marussi, M. Towrie, R.C. Atwood, P.J. Withers, P.D. Lee, The effect of powder oxidation on defect formation in laser additive manufacturing, Acta Mater. 166 (2019) 294–305. https://doi.org/10.1016/j.actamat.2018.12.027.

[4] K. Kakehi, S. Banoth, Y.L. Kuo, S. Hayashi, Effect of yttrium

addition on creep properties of a Ni-base superalloy built up by selective laser melting, Scr Mater. 183 (2020) 71–74. https://doi.org/10.1016/j.scriptamat.2020.03.014.
[5] K.T. Son, M.E. Kassner, K.A. Lee, The Creep Behavior of Additively Manufactured Inconel 625, Adv Eng Mater. 22 (2020). https://doi.org/10.1002/adem.201900543.
[6] K.S. Kim, T.H. Kang, M.E. Kassner, K.T. Son, K.A. Lee, High-temperature tensile and high cycle fatigue properties of inconel 625 alloy manufactured by laser powder bed fusion, Addit Manuf. 35 (2020) 101377. https://doi.org/10.1016/j.addma.2020.101377.
[7] K.T. Son, T.Q. Phan, L.E. Levine, K.S. Kim, K.A. Lee, M. Ahlfors, M.E. Kassner, The creep and fracture properties of additively manufactured inconel 625, Materialia (Oxf). 15 (2021) 101021. https://doi.org/10.1016/j.mtla.2021.101021.
[8] P.N. Quested, Modelling of Marangoni effects in electron beam melting, 1998. http://rsta.royalsocietypublishing.org/.
[9] R. Li, J. Liu, Y. Shi, L. Wang, W. Jiang, Balling behavior of stainless steel and nickel powder during selective laser melting process, International Journal of Advanced Manufacturing Technology. 59 (2012) 1025–1035. https://doi.org/10.1007/s00170-011-3566-1.
[10] M.E. Kassner, K.T. Son, K.A. Lee, T.H. Kang, R. Ermagan, The creep and fracture behavior of additively manufactured Inconel 625 and 718, Materials at High Temperatures. 00 (2022) 1–8. https://doi.org/10.1080/09603409.2022.2045101.
[11] T.D. McLouth, D.B. Witkin, J.R. Lohser, S.D. Sitzman, P.M. Adams, Z.R. Lingley, G.E. Bean, J.M. Yang, R.J. Zaldivar, Temperature and strain-rate dependence of the elevated temperature ductility of Inconel 718 prepared by selective laser melting, Materials Science and Engineering A. 824 (2021) 141814. https://doi.org/10.1016/j.msea.2021.141814.
[12] D. Deng, R.L. Peng, J. Moverare, High temperature mechanical integrity of selective laser melted alloy 718 evaluated by slow strain rate tests, Int J Plast. 140 (2021) 102974. https://doi.org/10.1016/j.ijplas.2021.102974.
[13] S. Floreen, J.M. Davidson, EFFECTS OF B AND Zr ON THE CREEP AND FATIGUE CRACK GROWTH BEHAVIOR OF A Ni-BASE SUPERALLOY., Metallurgical Transactions. A, Physical Metallurgy and Materials Science. 14 A (1983) 895–901. https://doi.org/10.1007/bf02644294.
[14] S. Yamaguchi, H. Kobayashi, T. Matsumiya, S. Hayami, Effect of minor elements on hot workability of nickel-base superalloys, Metals Technology. 6 (1979) 170–175. https://doi.org/10.1179/030716979803276110.
[15] F. Qi, L. Yu, G. Zhao, X. Xin, B. Zhang, W. Sun, Effect of Zr on solidification segregation behavior of K417G alloy and its anomalous effect during rapid cooling process, J Alloys Compd. 835 (2020) 155243. https://doi.org/10.1016/j.jallcom.2020.155243.
[16] F.C. Nunes, L.H. de Almeida, J. Dille, J.L. Delplancke, I. Le May, Microstructural changes caused by yttrium addition to NbTi-modified centrifugally cast HP-type stainless steels, Mater Charact.

58 (2007) 132–142. https://doi.org/10.1016/j.matchar.2006.04.007.
[17] S. Cao, Y. Yang, B. Chen, K. Liu, Y. Ma, L. Ding, J. Shi, Influence of yttrium on purification and carbide precipitation of superalloy K4169, J Mater Sci Technol. 86 (2021) 260–270. https://doi.org/10.1016/j.jmst.2021.01.049.
[18] Q. ling Li, H. rui Zhang, M. Gao, J. peng Li, T. xiao Tao, H. Zhang, Mechanisms of reactive element Y on the purification of K4169 superalloy during vacuum induction melting, International Journal of Minerals, Metallurgy and Materials. 25 (2018) 696–703. https://doi.org/10.1007/s12613-018-1617-4.
[19] S. Duan, J. Kang, J. Cho, M. Lee, W. Mu, J.H. Park, Manufacturing an ultra-low-sulfur CoCrFeMnNi high-entropy alloy by slagging through induction melting with ferroalloys feedstock, J Alloys Compd. 928 (2022) 167080. https://doi.org/10.1016/j.jallcom.2022.167080.
[20] P.D. Jablonski, J.J. Licavoli, M.C. Gao, J.A. Hawk, Manufacturing of High Entropy Alloys, Jom. 67 (2015) 2278–2287. https://doi.org/10.1007/s11837-015-1540-3.
[21] P.J. Zhou, J.J. Yu, X.F. Sun, H.R. Guan, X.M. He, Z.Q. Hu, Influence of Y on stress rupture property of a Ni-based superalloy, Materials Science and Engineering A. 551 (2012) 236–240. https://doi.org/10.1016/j.msea.2012.04.117.
[22] P.J. Zhou, J.J. Yu, X.F. Sun, H.R. Guan, Z.Q. Hu, Role of yttrium in the microstructure and mechanical properties of a boron-modified nickel-based superalloy, Scr Mater. 57 (2007) 643–646. https://doi.org/10.1016/j.scriptamat.2007.06.003.
[23] Z. Shi, S. Liu, M. Han, J. Li, Influence of yttrium addition on high temperature oxidation resistance of single crystal superalloy, Journal of Rare Earths. 31 (2013) 795–799. https://doi.org/10.1016/S1002-0721(12)60360-3.
[24] X. Li, S. He, J. Liang, X. Zhou, High-Temperature Oxidation Behavior and Oxide Scale Structure of Yttrium-Modified Ni–16Mo–7Cr–4Fe Superalloy at 1273 K, Oxidation of Metals. 92 (2019) 67–88. https://doi.org/10.1007/s11085-019-09914-0.
[25] A.V. Guimarães, R.M.S. da Silveira, L.H. de Almeida, L.S. Araujo, A.B. Farina, J.A. François Dille, Influence of yttrium addition on the microstructural evolution and mechanical properties of superalloy 718, Materials Science and Engineering A. 776 (2020). https://doi.org/10.1016/j.msea.2020.139023.
[26] W. Bian, H. Zhang, X. Zhang, M. Gao, J. Li, Q. Li, Y. Cui, H. Zhang, Comprehensive influence of Y on K417 superalloy: Purification, interactions among the alloy elements and high temperature properties, Materials Science and Engineering A. 755 (2019) 190–200. https://doi.org/10.1016/j.msea.2019.04.011.
[27] D.S. Kang, Y. Koizumi, K. Yamanaka, K. Aoyagi, H. Bian, A. Chiba, Significant impact of yttrium microaddition on high temperature tensile properties of Inconel 713C superalloy, Mater Lett. 227 (2018) 40–43. https://doi.org/10.1016/j.matlet.2018.03.106.
[28] Y. Wang, R. Ran, Y. Zhang, F. Fang, H. Wang, Y. Xia, G. Yuan, G. Wang, Materials Science & Engineering A Effects of yttrium

addition on microstructure and mechanical properties of Inconel 718 alloy produced by sub-rapid solidification, Materials Science & Engineering A. 823 (2021) 141726. https://doi.org/10.1016/j.msea.2021.141726.
[29] T. Naidu Palleda, S. Banoth, M. Tanaka, H. Murakami, K. Kakehi, The role of yttrium micro-alloying on microstructure evolution and high-temperature mechanical properties of additively manufactured Inconel 718, Mater Des. 225 (2023) 111567. https://doi.org/10.1016/j.matdes.2022.111567.
[30] L.Y. Wang, Z.J. Zhou, C.P. Li, G.F. Chen, G.P. Zhang, Comparative investigation of small punch creep resistance of Inconel 718 fabricated by selective laser melting, Materials Science and Engineering A. 745 (2019) 31–38. https://doi.org/10.1016/j.msea.2018.12.083.
[31] S. Sui, H. Tan, J. Chen, C. Zhong, Z. Li, W. Fan, A. Gasser, W. Huang, The influence of Laves phases on the room temperature tensile properties of Inconel 718 fabricated by powder feeding laser additive manufacturing, Acta Mater. 164 (2019) 413–427. https://doi.org/10.1016/j.actamat.2018.10.032.
[32] Y.L. Kuo, S. Horikawa, K. Kakehi, Effects of build direction and heat treatment on creep properties of Ni-base superalloy built up by additive manufacturing, Scr Mater. 129 (2017) 74–78. https://doi.org/10.1016/j.scriptamat.2016.10.035.
[33] S. Banoth, T.N. Palleda, T. Saito, H. Murakami, K. Kakehi, Creep anisotropy reduction and improvement via post-heat treatment in yttrium-added Hastelloy-X fabricated by laser powder bed fusion, International Journal of Advanced Manufacturing Technology. (2023) 1593–1609. https://doi.org/10.1007/s00170-023-11237-z.
[34] N. Hasani, C. Dharmendra, M. Sanjari, F. Fazeli, B.S. Amirkhiz, H. Pirgazi, G.D.J. Ram, M. Mohammadi, Laser powder bed fused Inconel 718 in stress-relieved and solution heat-treated conditions, Mater Charact. 181 (2021). https://doi.org/10.1016/j.matchar.2021.111499.
[35] L. Emanuelli, F. Deirmina, M. Pellizzari, Heat treatment behaviour of IN718 superalloy fabricated by laser-powder bed fusion, Mater Charact. 199 (2023). https://doi.org/10.1016/j.matchar.2023.112788.
[36] E. Bassini, G. Marchese, A. Aversa, Tailoring of the microstructure of laser powder bed fused inconel 718 using solution annealing and aging treatments, Metals (Basel). 11 (2021). https://doi.org/10.3390/met11060921.
[37] P.J. Zhou, J.J. Yu, X.F. Sun, H.R. Guan, X.M. He, Z.Q. Hu, Influence of Y on stress rupture property of a Ni-based superalloy, Materials Science and Engineering A. 551 (2012) 236–240. https://doi.org/10.1016/j.msea.2012.04.117.
[38] X. Hong, C.H. Hsueh, Effects of yttrium addition on microstructures and mechanical properties of CoCrNi medium entropy alloy, Intermetallics (Barking). 140 (2022) 107405. https://doi.org/10.1016/j.intermet.2021.107405.
[39] C. Kenel, A. De Luca, S.S. Joglekar, C. Leinenbach, D.C. Dunand, Evolution of Y2O3 dispersoids during laser powder bed fusion of

oxide dispersion strengthened Ni-Cr-Al-Ti γ/γ' superalloy, Addit Manuf. 47 (2021) 102224. https://doi.org/10.1016/j.addma.2021.102224.

[40] D. KANG, Effect of Yttrium Addition on Microstructure Evolution in Polycrystalline Inconel 713 Ni Based Superalloys, Tohoku University, 2018. https://ci.nii.ac.jp/naid/500001397813.bib (accessed December 24, 2023).

[41] K. Kakehi, S. Banoth, Y.L. Kuo, S. Hayashi, Effect of yttrium addition on creep properties of a Ni-base superalloy built up by selective laser melting, Scr Mater. 183 (2020) 71–74. https://doi.org/10.1016/j.scriptamat.2020.03.014.

[42] T.H. Hsu, K.C. Chang, Y.J. Chang, I.T. Ho, S. Tin, C.W. Li, K. Kakehi, C.P. Chen, K.K. Jen, H.Y. Hsieh, A.C. Yeh, Effect of Carbide Inoculants Additions in IN718 Fabricated by Selective Laser Melting Process, Minerals, Metals and Materials Series. (2020) 982–989. https://doi.org/10.1007/978-3-030-51834-9_96.

[43] H.U. Hong, I.S. Kim, B.G. Choi, M.Y. Kim, C.Y. Jo, The effect of grain boundary serration on creep resistance in a wrought nickel-based superalloy, Materials Science and Engineering A. 517 (2009) 125–131. https://doi.org/10.1016/j.msea.2009.03.071.

[44] Y.L. Kuo, T. Nagahari, K. Kakehi, The effect of post-processes on the microstructure and creep properties of Alloy718 built up by selective laser melting, Materials. 11 (2018). https://doi.org/10.3390/ma11060996.